J. Iron Steel Res. Int.
https://doi.org/10.1007/s42243-024-01194-6

ORIGINAL PAPER

Nanoindentation responses of NiCoFe medium-entropy alloys from cryogenic to elevated temperatures

Qin-qin Xu[1] · Kamran Karimi[1] · Amirhossein H. Naghdi[1] · Wen-yi Huo[1,2] · Chong Wei[3,4] · Stefanos Papanikolaou[1]

Received: 22 August 2023 / Revised: 23 November 2023 / Accepted: 26 November 2023

Abstract
NiCoFe alloy, a medium-entropy alloy, shows potential for applications in extreme environments. However, there is a theoretical barrier concerning the unclear understanding of its high-temperature dislocation motion mechanism. The load response exhibits distinct signatures relevant to thermal activation, most notably a decrease in critical force (i.e., softening) from cryogenic to elevated temperatures, e.g., from 200 to 1000 K. The onset of plasticity is characterized by the nucleation of stacking faults and prismatic loops at low temperatures, whereas the surface nucleation of Shockley partial dislocations dominates plasticity at elevated temperatures. We show that thermal effects lead to non-uniform atom pile-ups and control the rate of phase transformation with increasing indentation depth. The findings in this work extend the understanding of the mechanical response of NiCoFe alloys under indentation at different temperatures, shedding light on the underlying dislocation motion mechanisms and surface deformation characteristics. The observed transformation-induced plasticity mechanism has implications for the properties of medium-entropy alloys and their potential applications in extreme environments.

Keywords Orientation · Dislocations · Mechanical behaviors · Phase transition

1 Introduction

As a medium-entropy alloy (MEA), the equiatomic NiCoFe concentrated solid solution represents a very basic chemical composition that shows potential to exhibit outstanding thermo-mechanical properties under extreme environments, e.g., high strain rates, high temperature, corrosion, and irradiation [1–5]. These include, but are not limited to, single-phase thermodynamic stability [6] and high-temperature strength [7]) that often exceed those of conventional "dilute" alloys [8–10] with only one principal element. Such remarkable material properties have been commonly attributed to atomic-level chemical/micro-structural complexities in MEAs/high-entropy alloys (HEAs) that often interplay with (pre-)existing defects (i.e., point defects, dislocation lines, stacking faults) in a highly nonlinear and complex manner. At elevated temperatures, in particular, underlying deformation mechanisms such as dislocation nucleation, climb [11, 12], cross-slip [7, 13, 14], and glide dynamics [1, 13]) become extremely intricate in the presence of lattice disorder which may be conceptually thought as random pinning effects within a complex energy landscape [15]. Such deformation mechanisms are known to promote (or degrade) complex alloy performance, but their atomistic origins and direct relevance to bulk yielding properties have remained largely unexplored. Nanoindentation tests, as the gold standard in the field of nanomechanics, can provide rich

✉ Wen-yi Huo
wenyi.huo@ncbj.gov.pl

✉ Chong Wei
chong.wei@nwpu.edu.cn

✉ Stefanos Papanikolaou
stefanos.papanikolaou@ncbj.gov.pl

[1] NOMATEN Centre of Excellence, National Centre for Nuclear Research, Otwock 05-400, Mazowsze, Poland

[2] College of Mechanical and Electrical Engineering, Nanjing Forestry University, Nanjing 210037, Jiangsu, China

[3] Science and Technology on Thermo Structural Composite Materials Laboratory, Northwestern Polytechnical University, Xi'an 710072, Shaanxi, China

[4] School of Mechanics, Civil Engineering and Architecture, Northwestern Polytechnical University, Xi'an 710072, Shaanxi, China

Published online: 09 April 2024

knowledge and key insights into the nanoscopic origins of metal plasticity by directly probing their nano-mechanical response [16–20]. Atomistic modeling of materials under nanoindentation has also received great attention owing to its capability in combining nano-mechanical data and microstructural information with atomic-level accuracy, analogous to in situ electron microscopy techniques in real experiments [21–24]. Early numerical studies in this framework were primarily focused on crystal anisotropy effects on elastic–plastic response and associated defect nucleation and phase transformation in simulated pure metals [25, 26]. Within the context of chemically complex alloys, like NiCoFe, a special emphasis was given on chemical/micro-structural complexities and, in particular, lattice distortion effects on associated nano-mechanical response. For instance, Li et al. [27] employed molecular dynamics simulations to examine the elasto-plastic deformations of indentation in a FeCrCuAlNi HEA. Their findings revealed that the complex alloy possessed enhanced properties which can be ascribed to factors such as low stacking fault energy, dense atomic arrangement, and the presence of multiple phases for Fe within the multicomponent alloy. Along these lines, Hua et al. [28] reported relevant deformation mechanisms in a CoCrNi alloy under nanoindentation demonstrating that heterogeneous dislocation nucleation is enhanced by Cr-rich clusters, as opposed to the uniform nucleation observed in pure metals. The slow mobility of dislocations was further attributed to additional pinning effects characterized by high Peierls stresses, while nanotwins and phase transformations tend to occur at low temperature due to the low stacking fault energy. Additionally, at high temperature, the nucleation of distorted prismatic dislocation loops (PDLs) was shown to be assisted by a double-cross-slip mechanism. Similar observations were made in the work [29] reporting that the presence of chromium in face-centered cubic (FCC) FeNiCr multicomponent alloys reduces the mobility of PDLs and influences the density of geometrically necessary dislocations, leading to enhanced hardness and strain localization phenomena. However, there is still a lack of the information about the deformation mechanisms of medium-entropy alloys during nanoindentation over a wide temperature range.

Here, we focus on extensive molecular dynamics simulations of nanoindented NiCoFe alloy to understand how thermally activated mechanisms might influence dislocation plasticity taking into consideration the properties of the material as well as the role of external loading conditions. In this framework, we investigate the nano-mechanical response and dislocation behavior at different temperatures, playing a crucial role in determining the underlying nucleation, glide, and interaction mechanisms of dislocations. We observed that certain temperatures lead to the formation of unique dislocation structures and characteristics upon deformation, under the exact same loading conditions. Our comprehensive characterization of dislocation properties was based upon the use of detailed analysis techniques that capture distinct dislocation signatures in the presence of thermal activation. Through our dislocation analysis, we demonstrate that thermal effects significantly influence the surface morphology and local strains through the complex interplay of nucleated defects.

2 Computational methods

Molecular dynamics (MD) simulations are performed to investigate the deformation of NiCoFe alloy under nanoindentation using the opensource code LAMMPS [30]. All atomistic simulations are carried out using the modified embedded-atom method (MEAM) potential of Choi et al. [31], which has recently been used to investigate the effect of individual elements on solid solution hardening and reproduce the fundamental structural properties of advanced HEAs. A cut-off parameter for short-range interactions of 4.5 Å was used as in the original study of Choi et al. [31]. The NiCoFe sample is 42.4 nm × 40.6 nm × 37.0 nm and is divided into three sections along the Z [111] direction, which sets up a fixed boundary condition. [$\bar{1}01$] and Y [$1\bar{2}1$] are both periodic boundary conditions. The bottom frozen region ($0.02d_z$) ensures that the atoms are stable, and the thermostatic region ($0.08d_z$) dissipates the generated heat during nanoindentation, as shown in Fig. 1. The space between the tip and the top surface is 0.5 nm. After NiCoFe sample fabrication, the potential energy of the system is minimized using a force norm stopping criterion of 10^{-6} eV/Å. The samples are heated for 100 ps with a Langevin thermostat to temperatures of 200, 400, 600, 800, and 1000 K with a time constant of 100 fs. Then, the samples reached a homogeneous state. The last step is performed by relaxing the prepared sample for 10 ps to dissipate artificial heat, as shown in Fig. 1.

MD indentation simulations are performed at various temperatures using the procedure developed by Domínguez-Gutiérrez [32]. After sample equilibration, nanoindentation tests were performed using a spherical indenter tip. The total force F exerted by the indenter on the sample is defined by $F = -K\left(\overrightarrow{r}(t) - R\right)^2$, where K is the force field constant set to 236 eV/Å. $\overrightarrow{r}(t)$ and R refer to the position of the center of the tip as a function of time and radius, respectively. $\overrightarrow{r}(t) = x_0\overrightarrow{x} + y_0\overrightarrow{y} + (z_0 + zt)\overrightarrow{z}$, x_0 and y_0 present the center of the surface sample on the xy plane, and z_0 is the initial gap between the surface and the indenter tip moving with speed υ = 50 m/s. The loading and unloading processes are defined by considering the direction of the velocity as negative and positive,

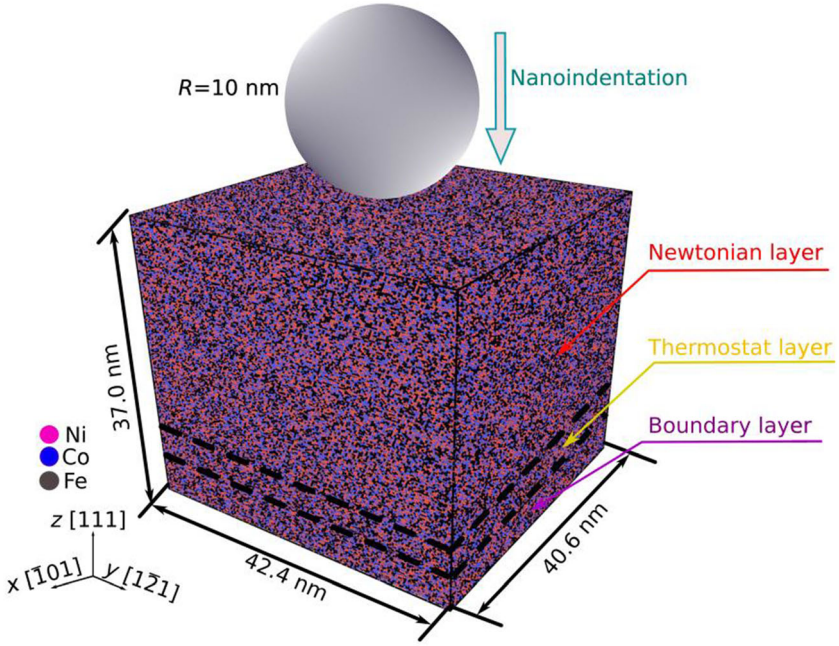

Fig. 1 Schematic of MD simulation model for nanocontact between a spherical indenter tip and a NiCoFe MEA sample

respectively. Each process is performed for 125 ps with a time step of Δt = 1 fs. The maximum indentation depth is chosen to be 2.1 nm to avoid the influence of boundary layers in the dynamical atom region.

In this study, the mechanical response of the NiCoFe sample is investigated for various temperatures and the Hertz model $F(\delta) = \frac{4}{3}E^* R^{\frac{1}{2}} \delta^{\frac{3}{2}}$, where E^* is the effective Young's modulus. R = 10 nm and δ is the indentation depth used to characterize the force response within the elastic regime of deformation [8]. The hardness of the indented sample is calculated by computing the $P-\delta$ curve with the method of Oliver and Pharr [33], following the fitting curve to the unloading process curve as:

$$P = P_0(\delta - \delta_f)^m \tag{1}$$

where P is the indentation load; δ_f is the residual depth after the whole indentation process; and P_0 and m are fitting parameters. Thus, the nanoindentation hardness (H) can be computed as

$$H = \frac{P_{max}}{A_c} \tag{2}$$

where P_{max} is the limited load force at the maximum indentation depth; $A_c = \pi(2R - \delta_c)\delta_c$ is the contact area with the tip; $\delta_c = \delta_{max} - \frac{\varepsilon P_{max}}{S}$; ε refers to the parameter of spherical indenter shape, ε= 0.75; S is the unloading stiffness; and δ_{max} is the maximum indentation depth. S is calculated as

$$S = \left(\frac{dP}{d\delta}\right)_{\delta=\delta_{max}} = mP_0(\delta_{max} - \delta_f)^{m-1} \tag{3}$$

Elementary shear processes are investigated using Ovito's DXA and grain identification algorithms.

3 Results and discussion

3.1 Mechanical response of NiCoFe sample under nanoindentation at various temperatures

Figure 2 displays the relationship between load and displacement as well as hardness versus displacement curves corresponding to the crystalline orientation [111] at various temperatures (T) of 200, 400, 600, 800, and 1000 K. All the indented samples accommodated deformation up to a prescribed displacement value of δ = 2 nm before they were unloaded to a zero-stress state. At T = 200 and 400 K, the load shows an overall increasing trend with depth throughout the indentation process (prior to unloading) as shown in Fig. 2a. In contrast, the mechanical response at T = 600, 800, and 1000 K exhibits non-monotonic features and is consistently characterized by a marked load drop following the elastic Hertz-like regime which is otherwise missing at the former temperatures. Nevertheless, the load response indicates distinct elastic and plastic regimes (irrespective of temperature) that are well separated by pop-in events and may be predicted theoretically by the Hertz

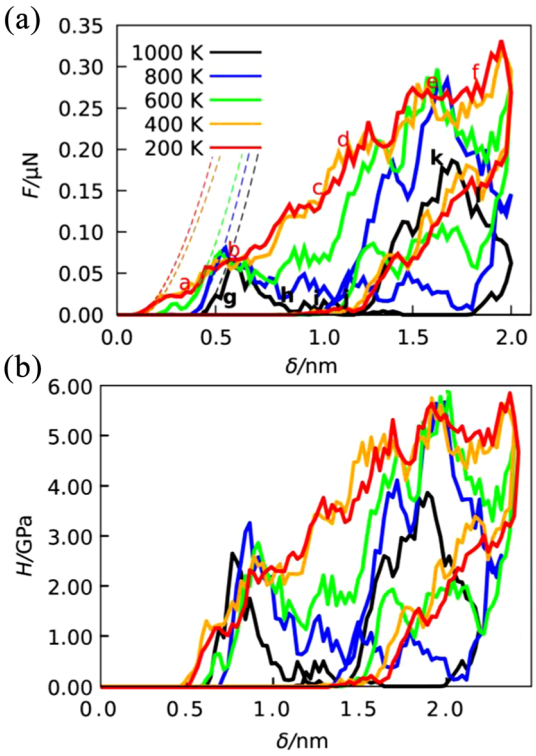

Fig. 2 Load–displacement curves (**a**) and hardness versus displacement plots (**b**) corresponding to NCoFe alloy under nanoindentation at crystal orientation [111]. Dashed curves indicate Hertz fits

model within the former regime. Within the plastic region, the observed discrepancy in the nano-mechanical response is indicative of emerging dislocations and/or nanotwins that tend to nucleate from the contacting surfaces and appear to have temperature-dependent deformation mechanisms associated with them. These observations will be further discussed in subsequent sections. Figure 2b also presents hardness versus displacement curves at different temperatures. Overall, the hardness data demonstrate very similar trends with the load curves. We note that while the maximum hardness of nearly 6 GPa seems to be fairly consistent at $T = 200$, 400, 600, and 800 K, it is notably smaller (approximately 4 GPa) at 1000 K, suggesting a fairly soft material response at this temperature.

Table 1 presents the inferred parameters obtained based on the Hertz fits including E, E^{f}, F_m, δ_c, and H_m. Based on these measurements, the largest F_m is determined at $T = 200$ K, suggesting the maximal resistance against deformation at the lowest temperature. And the largest E is attained at the lowest temperature $T = 200$ K.

3.2 Elementary deformation mechanisms

In Fig. 3, we probe distinct plastic deformation mechanisms associated with $T = 200$ and 1000 K, emphasizing the dislocation nucleation within the plastic zone and associated variations with temperature. At $T = 200$ K, the plastic deformation initially occurs at $\delta \approx 0.4$ nm, marked by "a" in Fig. 2a, which corresponds to $F \approx 0.33$ μN. At this stage, a perfect stacking fault tetrahedron (SFT) nucleates from the upper periphery of the indenter base, as illustrated in Fig. 3a. The SFT is characterized by two Shockley partial dislocations with Burgers vectors and one stair-rod dislocation with a Burgers vector [011] within {111}-family planes. The atomic configuration in the vicinity of the SFT compares very well with those reported in Ref. [34]. At a larger depth, $\delta = 0.8$ nm, a perfect dislocation and a few Shockley partial dislocations also appear as shown in Fig. 3b. Further, indentation up to $\delta = 1.0$ nm leads to the formation of basal dislocation loops around the central contact region, as illustrated in Fig. 3c. Subsequently, we observe the nucleation of the PDLs in Fig. 3d–f, as the loading continues. Figure 3d shows the development of an embryonic PDL as well as several gliding and interacting Shockley partials, forming a dislocation network. At a later stage in Fig. 3e, the Shockley partial dislocations gradually slip away from the indenter zone, and finally at $\delta = 1.8$ nm, the first prismatic loop begins to separate from the dislocation network as shown in Fig. 3f.

At $T = 1000$ K, the initial load drop at $\delta \approx 0.6$ nm is accompanied by the nucleation of Shockley partial dislocations from the surface region, as shown in Fig. 3g. These dislocations tend to escape rapidly from the indenter zone and glide within the sample, as shown in Fig. 3h–j,

Table 1 E^{*}, Hertz fitting intervals (E^{f}), critical load (F_m), depth (δ_c), and maximum hardness (H_m) for NiCoFe samples under indentation at various temperatures

T/K	E^{*}/GPa	E^{f}/nm	F_m/μN	δ_c/nm	H_m/GPa
200	325	0.10–0.21	0.33	1.95	5.70
400	315	0.09–0.23	0.32	1.95	5.63
600	305	0.35–0.46	0.30	1.63	5.81
800	300	0.38–0.52	0.28	1.68	5.63
1000	239	0.42–0.58	0.19	1.70	3.83

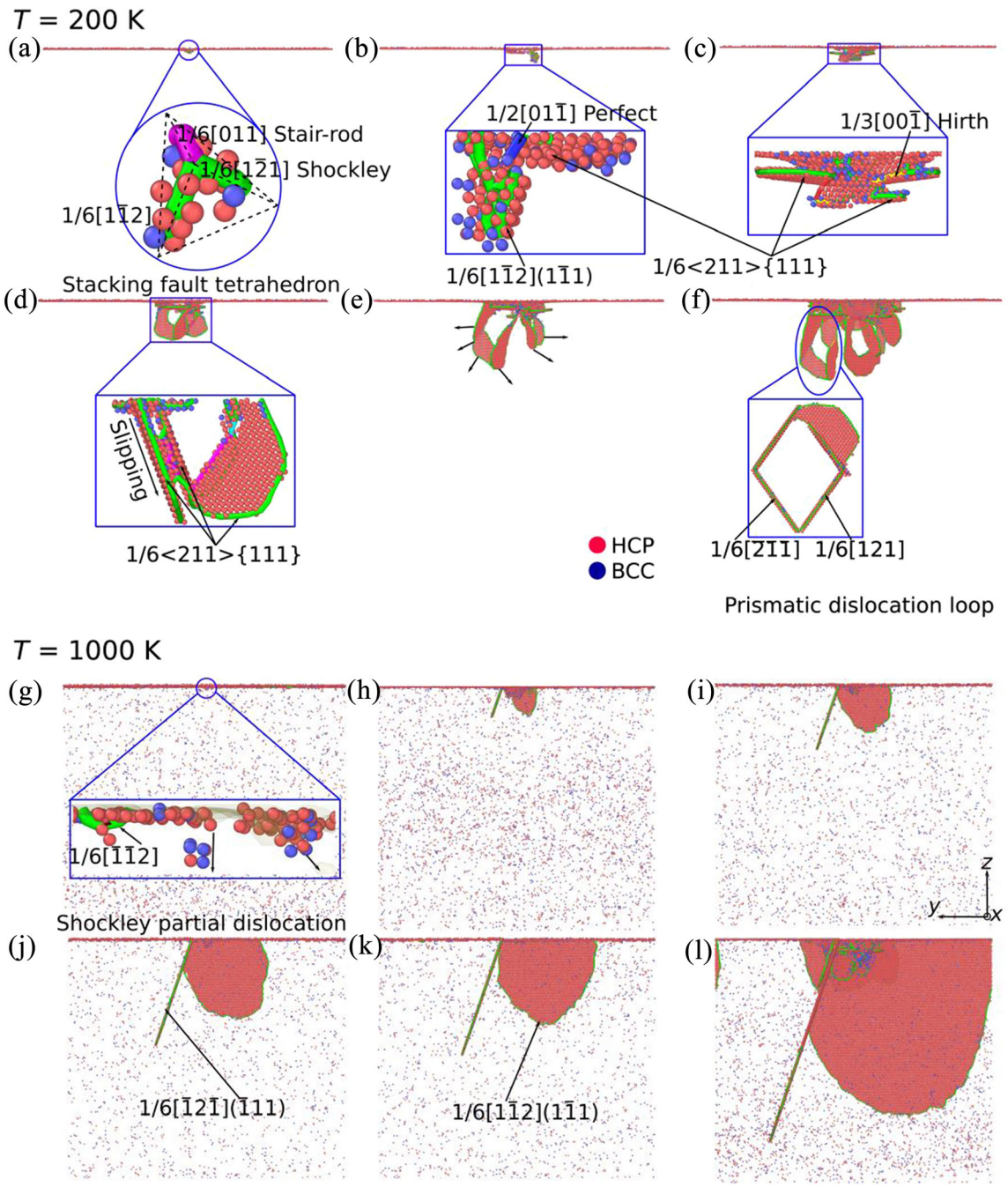

Fig. 3 Defect nucleation and evolution of NiCoFe alloy during nanoindentation at T = 200 and 1000 K corresponding to points marked in Fig. 2a

resulting in a relatively low force level. Following this regime, a renewed elastic loading process is observed that persists up to the next load drop occurring at $\delta \approx 1.6$ nm, as depicted in Fig. 3k. In comparison with T = 200 K, similar basal dislocation loops and gliding Shockley partial dislocations are nucleated around the indenter zone at 1000 K, as shown in Fig. 3l. Overall, the deformation processes observed at the above temperatures indicate fairly significant differences in terms of dislocation nucleation mechanisms and associated nano-mechanical response. At T = 200 K, various slip systems appear to be active, whereas at T = 1000 K, Shockley partial dislocations solely dominate the plastic response.

To gain further insights into the thermal effects on the mechanical response of NiCoFe alloy, we performed a detailed analysis of dislocations and atomic strain

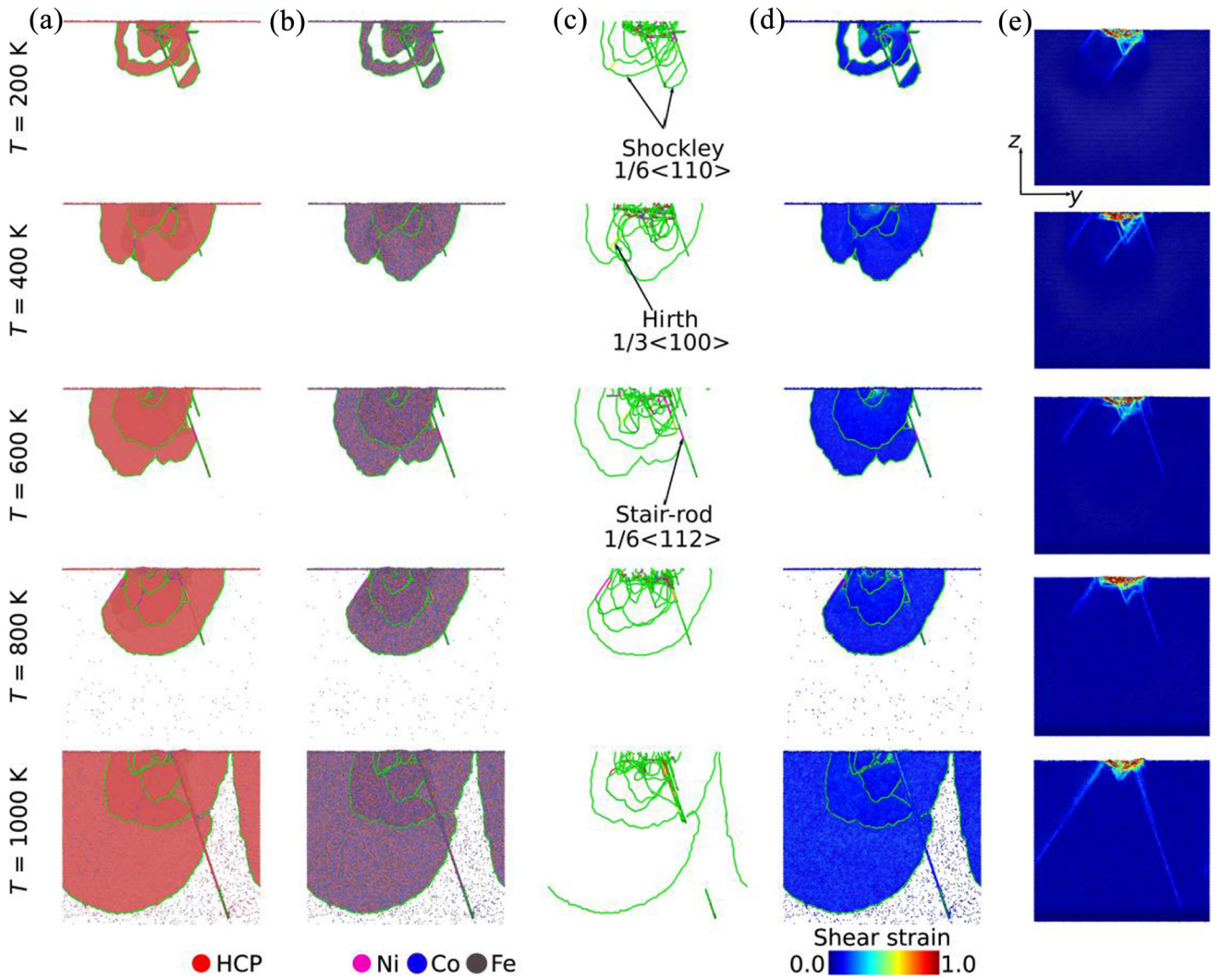

Fig. 4 Snapshots of defect structures (**a**), Ni, Co and Fe atoms and their distribution within stacking faults (**b**), dislocation loops (**c**), von Mises shear strain (**d**) and strain maps obtained near maximum depth $\delta = 2.0$ nm (**e**) at $T = 200$, 400, 600, 800, and 1000 K. Dislocation lines are colored based on their type including Shockley partials (blue), Hirth (light-yellow), and stair-rod (pink) dislocations

information. This analysis provides a better understanding of the topography of surface deformation and pileup which can be directly compared with experimental observations. Figure 4a illustrates the formation of planar defects within the indented sample. At $T = 200$ K, we observe an interconnected and densely populated defect network within the indenter zone. At elevated temperatures, thermal fluctuations assist deeper dislocation cross-slips, leading to the enlargement of the stacking faults. Figure 4b reveals randomly distributed Ni, Co, and Fe atoms within the stacking fault planes. Figure 4c presents the formation of dislocation loops at the maximum nanoindentation depth. The Hirth and stair-rod partial dislocations form due to the interaction of two partial dislocations described as:

$$\begin{cases} \frac{1}{6}[\bar{1}21] + \frac{1}{6}[1\bar{2}1] \rightarrow \frac{1}{3}[001] \\ \frac{1}{6}[\bar{1}2\bar{1}] + \frac{1}{6}[1\bar{1}2] \rightarrow \frac{1}{6}[011] \end{cases} \tag{4}$$

Figure 4d and e shows that the evolution of primary dislocations is accompanied by the nucleation of other similar dislocations and their propagation in different {111} planes through mechanisms like cross-slip. These dislocations are identified as partial dislocations, with a Burgers vector. As opposed to dislocation loops at $T = 200$ K, the higher temperature (at 1000 K) enhances the propagation of dislocation lines, resulting in the emergence of a larger plastic zone. It should also be noted that the shear strain continues to grow as the stacking fault planes glide at a faster rate. The stacking fault planes are moving or gliding through the crystal lattice more rapidly

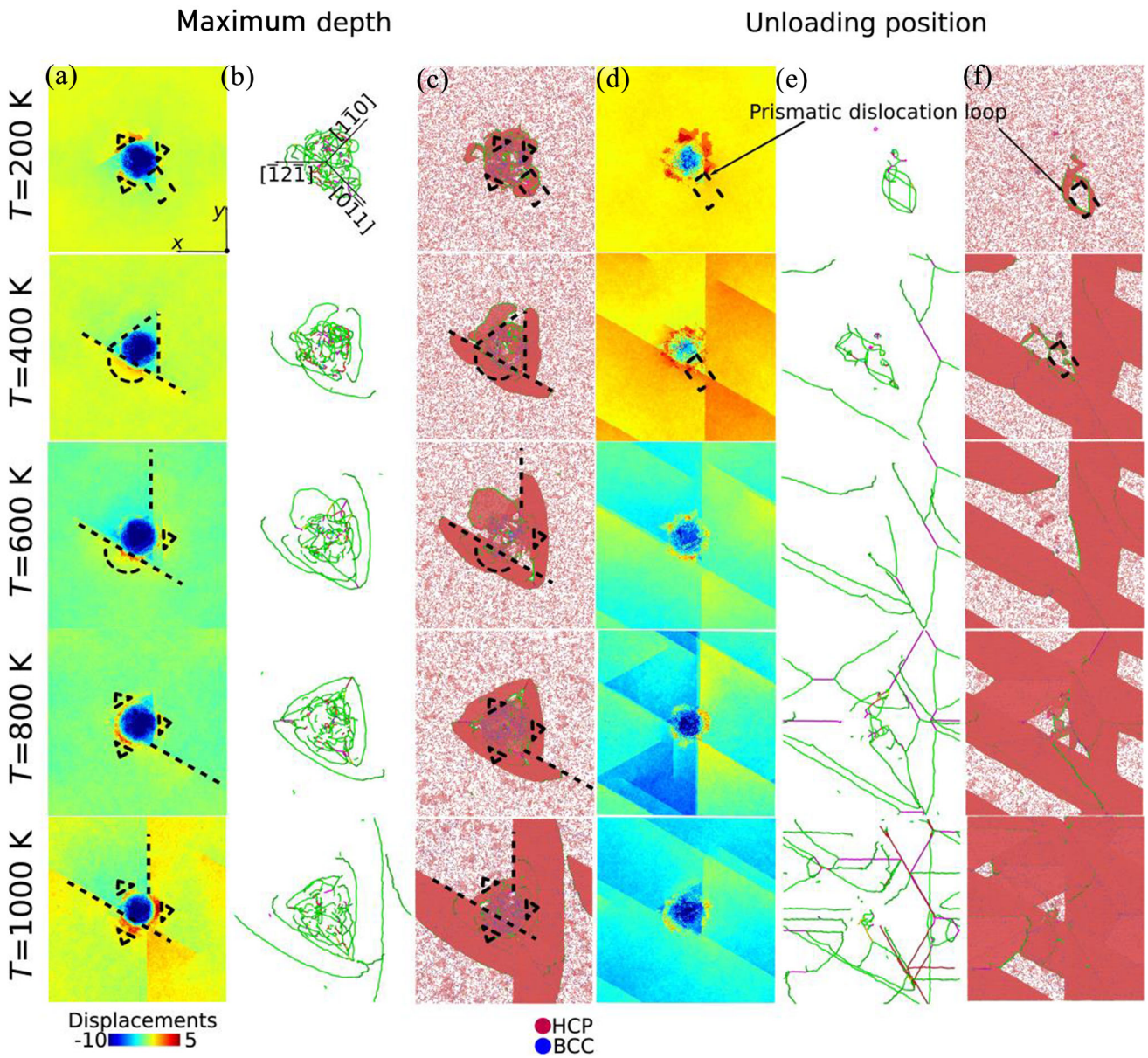

Fig. 5 Surface analysis at maximum indentation depth as well as unloaded sample at different temperatures on top view. **a**, **d** Atomic displacements (between − 10 and 5 Å); **b**, **e** formation and motion of dislocation loops; **c**, **f** gliding stacking fault planes on the top view

owing to the increased thermal activation. This increase in the mobility of stacking faults is evidenced in the snapshots of defect structures at the indenter depth of 2 nm presented in Fig. 4 where local shear strains feature deeper patterns within the bulk crystal with increasing temperature. Other relevant factors that can accelerate the gliding rate of the stacking fault planes include applied stress or material-specific microstructure.

Figure 5a shows the surface morphologies corresponding to the maximum depth at different temperatures. Here, the atoms are colored based on their height. As the temperature increases, the indentation groove gradually forms and more atoms tend to pile up on the surface of the sample, exhibiting highly non-uniform and asymmetrical features. Such features have also been observed in the nanoindentation of some HEAs [35, 36]. The development of larger grooves on the indented surface is owing to the significant movement of larger stacking fault planes along the slip direction parallel to the top surface T = 1000 K. By contrast, only a few dislocations move parallel to the top surface and mainly aggregate around the indenter, as shown in Fig. 5a at T = 200 K. Figure 5b shows the gliding loops along three directions $[\bar{1}2\bar{1}]$, $[1\bar{1}0]$ and $[0\bar{1}1]$. With increasing T, these loops symmetrically spread from the interconnected dislocation network and undergo dislocation cross-slip along the above orientations. Figure 5c

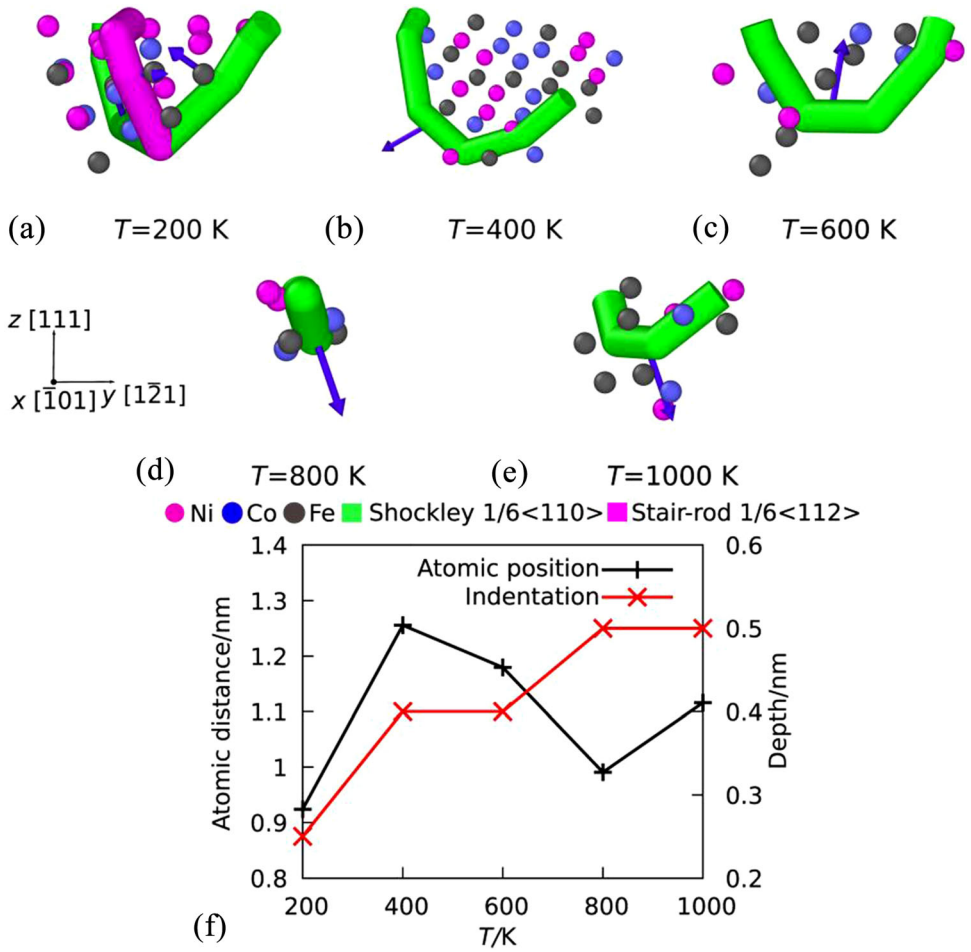

Fig. 6 Snapshots showing nucleation of initial dislocations for NiCoFe alloy at different temperatures (**a**–**e**) and indented depth of primary dislocation nucleation and deepest atomic position of dislocation loop as a function of various temperatures (**f**)

presents atomic information on defect nucleation and evolution and allows for a comparison with Fig. 5a and b. Figure 5d shows the surface morphologies corresponding to the unloading position at different temperatures. After removing the indenter, the interlocked dislocation network disappears within the plastic zone. The development of larger grooves on the indented surface depends on the formation of stable dislocation networks. The mirroring loops along the in-plane slip directions are vanishing, as shown in Fig. 5e. Figure 5f shows that the stable dislocations are tending to expand with increasing T upon unloading. A perfect embryonic PDL is observed at $T = 200$ K, while the unformed PDL surrounding with Shockley partial dislocations is visible at $T = 400$ K. It is worthy to noticing that the critical temperatures for the nucleation of stacking fault tetrahedra and prismatic dislocation loops are lower than 400 K, while the density of Shockley partial dislocations is enlarging sharply from $T = 400$ to 1000 K.

Figure 6a–e illustrates the nucleation of the primary dislocation loop from the surface. This initial plasticity mechanism agrees closely with the classical initial dislocation growth scheme proposed by Hua et al. [28] in pure Ni. They also reported the nucleation of dislocation loops from the NiCoCr surface. A high concentration of Fe atoms can be observed within the initial plastic zone, as shown in Fig. 6a–e, which could potentially reduce the yielding depth in MEAs and, therefore, favor the formation of defective embryos on the surface. Figure 6f plots the nucleation depth of the primary dislocation as well as the corresponding deepest atomic position as a function of T. Our data suggest that increasing the temperature does not significantly influence the initial dislocation nucleation, but instead affects the critical indentation depth.

Figure 7 plots the evolution of the number of hexagonal close-packed (HCP) atoms with the indentation depth. In the elastic regime, the original FCC lattice structure is preserved. Before the critical depth is reached (i.e., the first

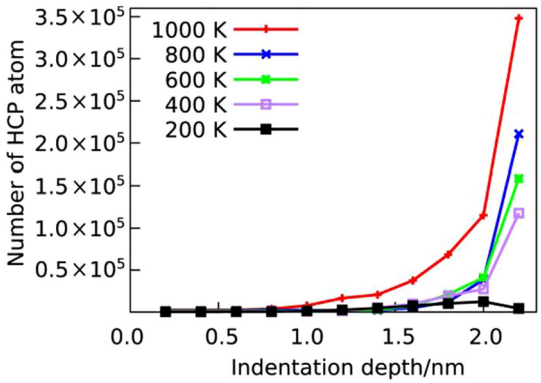

Fig. 7 Number of HCP atoms plotted against indentation depth at various temperatures

pop-in event at $\delta \approx 0.5$ nm), the HCP structure is not observed within this regime due to the absence of dislocations gliding into the sample, as shown in Fig. 7. At a later stage, plastic deformation initiates, which is accompanied by dislocation nucleation. Therefore, the number of HCP atoms increases sharply with the indentation depth. The number of HCP structures features a notable raise with increasing T, in comparison with the values observed at $T = 200$ and 1000 K. Upon unloading, the number of HCP atoms still grows rapidly regardless of $T = 200$ K. The number of HCP structures decreases remarkably because of the vanishing dislocation network and the remaining PDL within the inner zone of the sample as shown in Fig. 5f at $T = 200$ K. In contrast, the former continues to grow at higher temperatures owing to the progressive nucleation of stable dislocation loops as illustrated in Fig. 5f from $T = 400$ to 1000 K.

4 Conclusions

To conclude, we investigated the mechanical response of NiCoFe alloys under indentation at different temperatures. The load–displacement curves feature relevant signatures of thermal activation, particularly the decreasing critical force with elevated temperatures. We observed temperature-dependent dislocation-based mechanisms exhibiting various dislocation nucleation, glide, and interaction mechanisms. The plasticity at the lowest temperature $T = 200$ K was shown to involve the nucleation of stacking fault tetrahedra as well as prismatic loops. At the highest temperature $T = 1000$ K, on the other hand, the surface nucleation of Shockley partials dominated the plastic response. Correspondingly, the elastic modulus decreases from 325 GPa (200 K) to 239 GPa (1000 K). The thermal activation was also shown to have an effect on the surface morphology. As the temperature increases, the indentation groove gradually forms and more atoms tend to pile up on the sample surface, exhibiting highly non-uniform and asymmetrical features. The findings in this work extend the understanding of the mechanical response of NiCoFe alloys under indentation at different temperatures, shedding light on the underlying dislocation motion mechanisms and surface deformation characteristics. The observed transformation-induced plasticity mechanism has implications for the properties of medium-entropy alloys and their potential applications in extreme environments.

Acknowledgements We acknowledge support from the European Union Horizon 2020 research and innovation program under grant agreement No. 857470 and from the European Regional Development Fund via the Foundation for Polish Science International Research Agenda PLUS program grant No. MAB PLUS/2018/8. The publication was created within the framework of the project of the Minister of Science and Higher Education "Support for the activities of Centres of Excellence established in Poland under Horizon 2020" under contract No. MEiN/2023/DIR/3795. We acknowledge the computational resources provided by the High Performance Cluster at the National Centre for Nuclear Research in Poland.

Declarations

Conflict of interest Wen-yi Huo is a youth editorial board member for *Journal of Iron and Steel Research International* and was not involved in the editorial review or the decision to publish this article. The authors declare that there is no conflict of interest.

References

[1] C. Lu, L. Niu, N. Chen, K. Jin, T. Yang, P. Xiu, Y. Zhang, F. Gao, H. Bei, S. Shi, M.R. He, I.M. Robertson, W.J. Weber, L. Wang, Nat. Commun. 7 (2016) 13564.
[2] A.R. Cui, S.C. Hu, S. Zhang, J.C. Cheng, Q. Li, J.Y. Huang, S.N. Luo, Int. J. Mech. Sci. 252 (2023) 108331.
[3] T. Zhang, S. Ma, D. Zhao, Y. Wu, Y. Zhang, Z. Wang, J. Qiao, Int. J. Plast. 124 (2020) 226–246.
[4] F. Tuomisto, I. Makkonen, J. Heikinheimo, F. Granberg, F. Djurabekova, K. Nordlund, G. Velisa, H. Bei, H. Xue, W.J. Weber, Y. Zhang, Acta Mater. 196 (2020) 44–51.
[5] W. Huo, S. Wang, F. Fang, S. Tan, Ł. Kurpaska, Z. Xie, H.S. Kim, J. Jiang, J. Mater. Res. Technol. 20 (2022) 1677–1684.
[6] Y. Zhang, Y.N. Osetsky, W.J. Weber, Chem. Rev. 122 (2022) 789–829.

[7] K. Lu, A. Chauhan, D. Litvinov, M. Walter, A.S. Tirunilai, J. Freudenberger, A. Kauffmann, M. Heilmaier, J. Aktaa, Mater. Sci. Eng. A 791 (2020) 139781.
[8] K.L. Johnson, K.L. Johnson, Contact mechanics, Cambridge university press, Cambridge, UK, 1987.
[9] X. He, L. Liu, T. Zeng, Y. Yao, Int. J. Mech. Sci. 177 (2020) 105567.
[10] K. Yuan, X. Yao, Y. Yu, R. Wang, Z. Chai, K. Zhou, Z. Wang, Int. J. Mech. Sci. 246 (2023) 108148.
[11] S. Zhao, G.M. Stocks, Y. Zhang, Acta Mater. 134 (2017) 334–345.
[12] M. Jin, P. Cao, M.P. Short, Acta Mater. 147 (2018) 16–23.
[13] M. Sudmanns, J.A. El-Awady, Acta Mater. 220 (2021) 117307.
[14] Z.Y. Jia, S.Z. Zhang, J.T. Huo, C.J. Zhang, L.W. Zheng, F.T. Kong, H. Li, Mater. Sci. Eng. A 834 (2022) 142617.
[15] W. Li, S. Lyu, Y. Chen, A.H.W. Ngan, PNAS 120 (2023) e2209188120.
[16] Z. Yin, X. Liu, N. Gao, S. Li, J. Yao, Z. Fan, W. Zhang, Y. Wang, J. Alloy. Compd. 951 (2023) 169966.
[17] Q. Liu, J. Y. Hua, Y. F. Xu, K. Yang, J. C. Cheng, N. B. Zhang, C. Li, Y. Cai, S. N. Luo, Int. J. Mech. Sci. 249 (2023) 108252.
[18] W. Huo, F. Fang, X. Liu, S. Tan, Z. Xie, J. Jiang, Appl. Phys. Lett. 114 (2019) 101904.
[19] M. Yang, J.X. Wang, Trans. Nonferrous Met. Soc. China 33 (2023) 2417–2427.
[20] E.J. Chun, N.H. Kang, Y.H. Park, M.B. Moon, J.Y. Kang, J. Iron Steel Res. Int. 18 (2011) No. S1, 310–311.
[21] S.Z. Chavoshi, S. Xu, Prog. Mater. Sci. 100 (2019) 1–20.
[22] T. Gao, H. Song, B. Wang, Y. Gao, Y. Liu, Q. Xie, Q. Chen, Q. Xiao, Y. Liang, Int. J. Mech. Sci. 237 (2023) 107800.
[23] S. Liu, G. Feng, L. Xiao, Y. Guan, W. Song, Int. J. Mech. Sci. 239 (2023) 107859.
[24] Z.N. Zhang, Y.L. Li, W.P. Wu, Trans. Nonferrous Met. Soc. China 32 (2022) 206–216.
[25] C. Begau, A. Hartmaier, E.P. George, G.M. Pharr, Acta Mater. 59 (2011) 934–942.
[26] T.P. Remington, C.J. Ruestes, E.M. Bringa, B.A. Remington, C.H. Lu, B. Kad, M.A. Meyers, Acta Mater. 78 (2014) 378–393.
[27] J. Li, Q. Fang, B. Liu, Y. Liu, Y. Liu, J. Micromech. Mol. Phys. 1 (2016) 1650001.
[28] D. Hua, Q. Xia, W. Wang, Q. Zhou, S. Li, D. Qian, J. Shi, H. Wang, Int. J. Plast. 142 (2021) 102997.
[29] F.J. Dominguez-Gutierrez, A. Ustrzycka, Q.Q. Xu, R. Alvarez-Donado, S. Papanikolaou, M.J. Alava, Model. Simul. Mater. Sci. Eng. 30 (2022) 085010.
[30] S. Plimpton, J. Comput. Phys. 117 (1995) 1–19.
[31] W.M. Choi, Y.H. Jo, S.S. Sohn, S. Lee, B.J. Lee, NPJ Comput. Mater. 4 (2018) 1.
[32] F.J. Domínguez-Gutiérrez, S. Papanikolaou, A. Esfandiarpour, P. Sobkowicz, M. Alava, Mater. Sci. Eng. A 826 (2021) 141912.
[33] W.C. Oliver, G.M. Pharr, J. Mater. Res. 7 (1992) 1564–1583.
[34] S. Hu, T. Fu, Q. Liang, S. Weng, X. Chen, Y. Zhao, X. Peng, Front. Mater. 8 (2022) 813382.
[35] Y. Chen, Y. Fang, X. Fu, Y. Lu, S. Chen, H. Bei, Q. Yu, J. Mater. Sci. Technol. 73 (2021) 101–107.
[36] L. Kurpaska, F.J. Dominguez-Gutierrez, Y. Zhang, K. Mulewska, H. Bei, W.J. Weber, A. Kosińska, W. Chrominski, I. Jozwik, R. Alvarez-Donado, S. Papanikolaou, J. Jagielski, M. Alava, Mater. Des. 217 (2022) 110639.